Geochemistry, Geophysics, Geosystems

RESEARCH ARTICLE
10.1029/2018GC008167

Key Points:
- A magnetotelluric survey was collected over the Chilean subduction zone at 36 degrees south in order to map geoelectric structure
- Conductors show important dehydration reactions along plate interface as well as important zones of crustal melt beneath the volcanic arc
- Correlations with previous seismic results show a possible asperity on plate interface, which may influence megathrust rupture

Supporting Information:
- Supporting Information S1

Correspondence to:
D. Cordell,
dcordell@ualberta.ca

Citation:
Cordell, D., Unsworth, M. J., Diaz, D., Reyes-Wagner, V., Currie, C. A., & Hicks, S. P. (2019). Fluid and melt pathways in the central Chilean subduction zone near the 2010 Maule earthquake (35–36°S) as inferred from magnetotelluric data. *Geochemistry, Geophysics, Geosystems*, *20*, 1818–1835. https://doi.org/10.1029/2018GC008167

Received 27 DEC 2018
Accepted 27 MAR 2019
Accepted article online 1 APR 2019
Published online 11 APR 2019

Fluid and Melt Pathways in the Central Chilean Subduction Zone Near the 2010 Maule Earthquake (35–36°S) as Inferred From Magnetotelluric Data

Darcy Cordell[1], Martyn J. Unsworth[1], Daniel Diaz[2], Valentina Reyes-Wagner[2], Claire A. Currie[1], and Stephen P. Hicks[3]

[1]Department of Physics, University of Alberta, Edmonton, Alberta, Canada, [2]Departamento de Geofísica, Universidad de Chile, Santiago, Chile, [3]Department of Ocean and Earth Sciences, University of Southampton, Southampton, UK

Abstract The subduction zone of central Chile (36°S) has produced some of the world's largest earthquakes and significant volcanic eruptions. Understanding the fluid fluxes and structure of the subducting slab and overriding plate can provide insight into the tectonic processes responsible for both seismicity and magmatism. Broadband and long-period magnetotelluric data were collected along a 350-km profile in central Chile and Argentina and show a regional geoelectric strike of 15 ± 19° east of north. The preferred two-dimensional inversion model included the geometry of the subducting Nazca plate as a constraint. On the upper surface of the Nazca plate, conductors were interpreted as fluids expelled from the downgoing slab via compaction at shallow depth (C1) and metamorphic reactions at depths of 40–90 km (C2 and C3). At greater depths (130 km), a conductor (C7) is interpreted as a region of partial melt related to deserpentinization in the backarc. A resistor on the slab interface (R1) is coincident with a high-velocity anomaly which was interpreted as a strong asperity which may affect the coseismic slip behavior of large megathrust earthquakes at this latitude. Correlations with seismicity suggest slab fluids alter the forearc mantle and define the downdip limit of the seismogenic zone. Beneath the volcanic arc, several upper crustal conductors (C4 and C5) represent partial melt beneath the Tatara-San Pedro Volcano and the Laguna del Maule Volcanic Field. A deeper lower crustal conductor (C6) underlies both volcanoes and suggests a connected network of melt in a thermally mature lower crust.

Plain Language Summary Central Chile has experienced some of the world's largest earthquakes and many large volcanic eruptions. These disasters are caused by the tectonic processes in this region as the oceanic Nazca plate subducts beneath the South American plate. As the oceanic plate subducts, water is released, which can increase pressure, lubricate the plates, and lower rock melting points to produce magma. As such, fluids are an important control on where earthquakes and volcanoes occur. We image the electrical conductivity of this region using the magnetotelluric method since saline water and/or partial melt both have a high conductivity. Several conductors are imaged near the plate interface that can be related to presence of water or partial melt. Correlations between the locations of conductors and zones of low seismic velocity reported in previous seismic studies support the idea that there is an anomalous block of rock at 30-km depth, which increases friction along the subducting plate interface. This could explain why the 2010 Maule earthquake did not rupture far inland. A conductor at 40-km depth correlates with a gap between two clusters of earthquakes, which suggests that fluids may chemically alter the continental plate and reduce friction in this gap.

1. Introduction

Subduction zone margins account for the majority of global volcanic hazards and include many earthquake-prone areas. It has been recognized that water and hydrated minerals play a vital role in magma generation and seismicity at subduction zones (Stern, 2002). Various numerical simulations and laboratory studies suggest that phase transitions of these hydrated minerals are responsible for the upward migration of water-rich melt into the overriding crust (e.g., Grove et al., 2012; Hacker, 2008; Petrelli et al., 2018). These fluids then lower the solidus temperature of the surrounding mantle rocks, generating hydrous mafic melts. Determining the amount of water, the depth at which it is released, and the zones of accumulation of

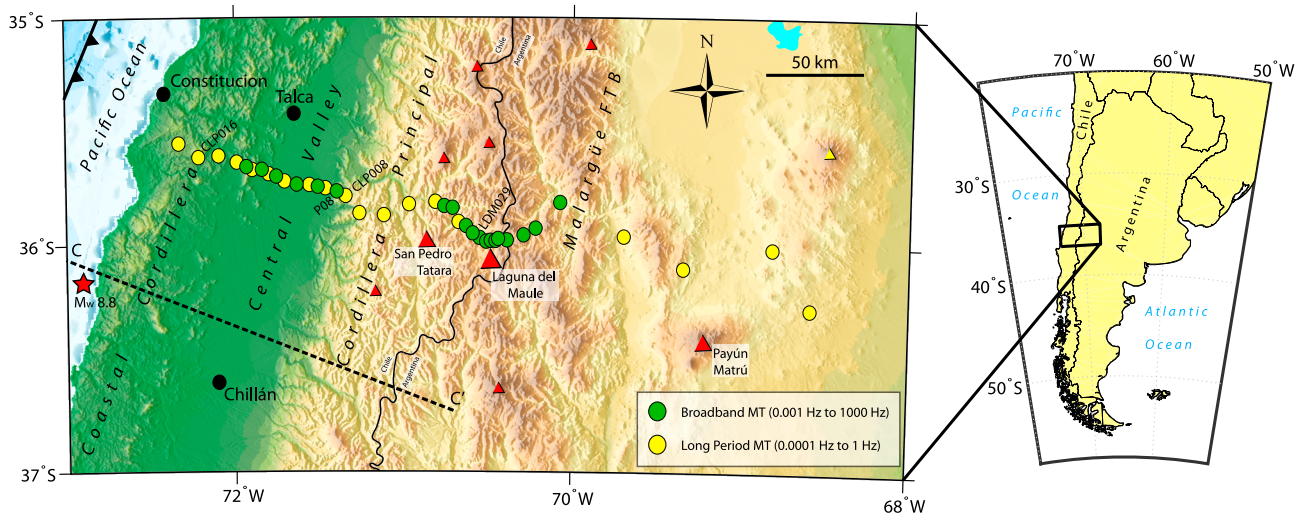

Figure 1. Study area in central Chile and western Argentina. Yellow and green circles denote long-period and broadband magnetotelluric site locations, respectively. Red triangles show the locations of significant volcanoes in the Cordillera Principal. The red star shows the epicenter location of the 2010 M_w 8.8 Maule earthquake. An inset map of southern South America on the right shows the location of the study area within the black box. Important towns are shown as black circles. Important volcanoes mentioned in the text are labeled (San Pedro-Tatara, Laguna del Maule, and Payún Matrú). Stations shown in Figure 3 are labeled. Profile C–C′ denotes the seismic velocity profile shown in Figure 6 from Hicks et al. (2014). Malargüe FTB = Malargüe Fold and Thrust Belt; MT = magnetotelluric.

aqueous fluids and partial melt are critical parameters in examining magma flux and magma genesis (Petrelli et al., 2018; Völker & Stipp, 2015). Furthermore, it has been widely suggested that fluids control the distribution of seismic and aseismic zones within a subduction zone and thus understanding seismicity and fluid relationships is important (Saffer, 2017).

The magnetotelluric (MT) method has been used to image a number of subduction zones including Cascadia (McGary et al., 2014; Wannamaker et al., 2014), Costa Rica (Worzewski et al., 2011), southern Mexico (Jödicke et al., 2006), Japan (Hata et al., 2015), New Zealand (Heise et al., 2017; Wannamaker et al., 2009), and the Central Andes (Brasse & Eydam, 2008; Unsworth et al., 2018; Vargas et al., 2019). This method is useful in these studies of subduction zone processes because the presence of interconnected aqueous fluids and/or partial melts increases the conductivity of both crustal and mantle rocks. The MT studies of subduction zones have highlighted that there is great variability in electrical structure showing shallow (<15 km) conductors associated with expulsion of fluid from pore spaces and mantle wedge conductors (~50 km) that have been related to the addition of fluids derived from the metamorphic transition of the downgoing slab from basalt to eclogite (Pommier & Evans, 2017). A deeper conductor within the mantle wedge (>60 km) is sometimes observed and is formed as water is released by the breakdown of serpentine that can lead to partial melting in the mantle wedge (e.g., McGary et al., 2014). This suggests significant along-strike variations related to the incoming plate properties (e.g., fractures, serpentinization, and temperature) that may be related to structures such as seamounts and plate age as well as the structure of the upper plate mantle wedge (Pommier & Evans, 2017).

In the Maule Region of the Chilean subduction zone at 35°S to 37°S (Figure 1), the Nazca plate subducts obliquely beneath the South American plate at 6 to 8 cm/year driving regional volcanism in the Southern Volcanic Zone (Angermann et al., 1999). The Maule region is approximately 600 km south of the Pampean flat slab segment and the subducting slab in the Maule region descends at an angle of approximately 30° (Pesicek et al., 2012). This region has seen significant damage from megathrust earthquakes in the last decade (e.g., 2010 M_w 8.8 and 2012 M_w 7.1) as well as a large M_w 8.3 intraslab earthquake in 1939 near Chillán (Moreno et al., 2012; Ruiz & Madariaga, 2018). There have also been significant volcanic eruptions in the last century at edifices on the volcanic arc (Figure 1; Völker et al., 2011). The backarc Laguna del Maule Volcanic Field (LdMVF) is currently showing signs of unrest with unprecedented, long-term upward ground deformation at velocities greater than 20 cm/year for over 10 years (Feigl et al., 2013; Le Mével et al., 2015). Furthermore, there appear to be stress-state linkages between tectonic events near the trench and shallow deformation at nearby volcanoes (Le Mével et al., 2015; Pritchard et al., 2013). In the backarc,

there is a unique concentration of Pleistocene and Holocene basalt flows within the Payenia volcanic province in western Argentina suggesting an anomalously hot sublithospheric region nearly 200 km east of the modern volcanic arc (Ramos & Folguera, 2011). The structure of Payenia has been imaged by previous 3-D MT studies in Argentina (Burd et al., 2014). The unique volcanism and seismicity of the Maule Region shows that this is an active corridor in the Andean subduction system, which requires further study in order to determine the subduction zone structure and fluid fluxes. Numerical studies by Völker and Stipp (2015) have shown significant along-strike variations in fluid flux in the Chilean Andes, which they interpreted to be primarily controlled by the thermal state of the incoming Nazca plate. They suggest the main control on this variation is the age of the Nazca plate, which increases northward, although sedimentation or hydrothermal circulation may also play a role. Previous passive seismic studies have shown low velocity regions coinciding with fluids as well as anomalously high-velocity regions on the plate interface which may be asperities that encourage plate locking, affecting the slip distribution of megathrust earthquakes (Hicks et al., 2012, 2014). Asperities and pore fluid pressures have also been linked to the recurrence intervals for large megathrust earthquakes in Chile (Moreno et al., 2018) as well as other subduction zones (e.g., Schellart & Rawlinson, 2013). Therefore, understanding fluid fluxes and asperities in this region is important.

The South American plate at this latitude can be divided into four broad geological units from west to east (Figure 1). Along the Pacific Ocean, the Coastal Cordillera consists primarily of outcrops of Paleozoic metamorphic rocks from ancient accretionary wedge complexes (Hervé et al., 2013). To the east, the Central Valley is a 70-km-wide depression filled with 500-m-thick Quaternary sediments and ignimbritic cover (Farías et al., 2008). The Principal Cordillera is a 60-km-wide mountain range, which consists of Mesozoic-to-Cenozoic volcanic sequences and exposed plutons as well as modern Quaternary volcanic edifices such as Tatara-San Pedro (TSP) and Cerro Azul (Hildreth & Moorbath, 1988; Singer et al., 1997). Finally, to the east in the backarc region is the Malargüe fold and thrust belt, which includes deformed Mesozoic units and the front ranges of the eastern Andes (Ramos et al., 2014). Between the Malargüe fold and thrust belt and the Principal Cordillera is the hypothesized northwest trending Las Loicas trough, which includes numerous calderas and volcanic fields such as Calabozos, Puelche, and the LdMVF (Ramos et al., 2014). The current geometry is one of normal subduction as shown by regional teleseismic studies (Pesicek et al., 2012). However, a flat slab was present at this location (5–3 Ma) and steepened around 2 Ma (Ramos et al., 2014). As the slab flattened between 14 and 10 Ma, the arc migrated into the foreland and expanded before arc magmatism stopped almost entirely for 2 Ma (Ramos et al., 2014). The most recent steepening cycle has led to increased volcanism once again including many Quaternary rhyolite calderas and flood basalts. It is suggested that the process of steepening may still be ongoing (Ramos et al., 2014).

In this study, MT data collected between 2016 and 2017 are used to model the distribution of fluids and partial melt from the Chilean coast into western Argentina along a two-dimensional (2-D) profile perpendicular to the trench. Two-dimensional isotropic inversion is employed, and additional information from previous seismic studies is incorporated into an integrated interpretation.

2. Methods and Data Analysis

The MT method images subsurface conductivity structure using naturally occurring, plane wave electromagnetic (EM) signals to induce electric currents in the Earth (Chave & Jones, 2012). In the frequency domain, the electric and magnetic field components can be related via an impedance tensor, which is sensitive to Earth conductivity structure with lower frequencies sampling greater depths. In general, the Earth's conductivity structure is three dimensional and the impedance tensor has complex values and is a full 2×2 matrix. However, if the Earth has a 2-D structure, where the conductivity does not vary in the geoelectric strike direction, the diagonal components of the tensor are 0 when the coordinate system is parallel to the strike direction. In this case, Maxwell's equations decouple into two independent modes, the transverse magnetic (TM) mode and the transverse electric (TE) mode. In many applications, a 2-D assumption can be valid if the impedance tensor data are rotated so that the diagonal components are minimized.

In 2016, broadband MT data (0.001- to 1000-Hz frequency response) were collected along a profile that extended from the Central Valley to the Argentine border perpendicular to the trench (Reyes-Wagner et al., 2017; Figure 1). This profile included some additional MT data collected between 2009 and 2016

(Cordell et al., 2018; Hickson et al., 2011). However, the profile only measured broadband MT data and was only able to reliably image the upper 30 km of the crust. In order to measure the longer periods needed to image the deeper parts of the subduction zone in the lower crust, mantle, and subducting slab, 15 additional long-period MT stations were collected in 2017 using the Narod Intelligent Magnetotelluric Systems data logger, Pb-$PbCl_2$ electrodes and fluxgate magnetometers. Additionally, four broadband MT stations were collected in western Argentina using the Metronix ADU-07 data logger to extend the profile eastward into the backarc and four long-period Narod Intelligent Magnetotelluric Systems stations were included from the study of Burd et al. (2014) in western Argentina (Figure 1). The long-period sites recorded time series data for between 5 and 23 days, and the robust data processing methods of Egbert and Booker (1986) were applied using remote reference techniques where synchronous data were available. The broadband MT data were measured for between 12 and 48 hr, and time series were processed using the robust methods with smoothing constraints of Larsen et al. (1996). In total, 38 sites were included along a profile trending N105°E (Figure 1).

An analysis of the directionality and dimensionality of the impedance tensor data was carried out to determine if a 2-D assumption was valid for modeling the subsurface conductivity along this profile. This was done using the tensor decomposition methods of McNeice and Jones (2001) as well as an analysis of the phase tensors (Caldwell et al., 2004). Multisite, multifrequency tensor decomposition shows a regional strike of N15°E ± 19° for periods >1 s, which is within error of the N5°E regional strike obtained using only broadband MT (Figure 2; Reyes-Wagner et al., 2017). Mean strike and one standard deviation uncertainty was estimated using directional statistics (Mardia, 1972) where one standard deviation in radians equals

$$\sigma = \frac{1}{4}\sqrt{-2\ln(\bar{r})}$$

where $\bar{r}$ is the mean resultant (i.e., the length of the vector of mean sine and mean cosine of the strike). The factor of 1/4 is necessary because the quadrant of the geoelectric strike is inherently ambiguous and requires further interpretation from geology. In our case, because the Andes run approximately north-south, the regional geoelectric strike was taken to be approximately north-south, rather than east-west.

There is a clear along-profile change in the geoelectric structure across the Cordillera Principal (Figure 2a). On the west side of the profile there is a well-defined strike of N15°E ± 4° while on the east side of the profile, the strike is much more poorly defined and oriented N27°W ± 26° with several stations in the Cordillera Principal having a strike direction near N60°E (or N30°W). This may be due to the ocean effect on the western side of the profile and more complicated geology (e.g., the northwest trending Las Loicas trough) affecting the regional picture on the eastern side of the profile (Ramos et al., 2014). It could also be a result of more short period data being available on the eastern side of the profile which samples smaller, local structures. High skew values ($\beta > 3°$) obtained from phase tensor analysis were observed at nearly all periods greater than 10 s, suggesting some significant 3-D effects at depth especially on the east side of the profile (Figure 2c; Booker, 2014). It is worth noting that inconsistent strike direction is not an indication of 3-D structure since most sites with inconsistent strike have low skew values and are located in the northwest trending Las Loicas trough.

Apparent resistivity and phase curves for the TE and TM modes are shown in supporting information Figure S1 where the tensor impedance data are rotated to the regional strike of N15°E. Pseudosection plots of the apparent resistivity and phase for rotated off-diagonal components of the impedance tensor are shown in Figure 3. Here, the main geological units can be seen in pseudosection: (1) The highly resistive metamorphic block of the Coastal Cordillera is seen in both apparent resistivity modes; (2) the more conductive volcaniclastic and sedimentary fill of the Central Valley; and (3) a generally conductive volcanic arc and backarc. The phase split is also apparent on the western side of the profile, which indicates an ocean effect as the TM mode tends to have very low phases (<10°) at long periods (>100 s), while the TE mode has moderate to high phases (>75°) at long periods. At very long periods (>2,000 s), some out of quadrant phases were observed which may suggest anisotropic structure, coastal effects, and/or complicated 3-D geometry (Heise & Pous, 2003; Selway et al., 2012). The fact that the profile is a mixture of both broadband MT and long-period MT is apparent in the pseudosection. There is an irregular sampling of different frequency bands with more long-period data on the western side of the profile (i.e., west of the Cordillera Principal), a bias toward higher frequencies in the middle of the profile (i.e., in the Cordillera Principal), and a return to

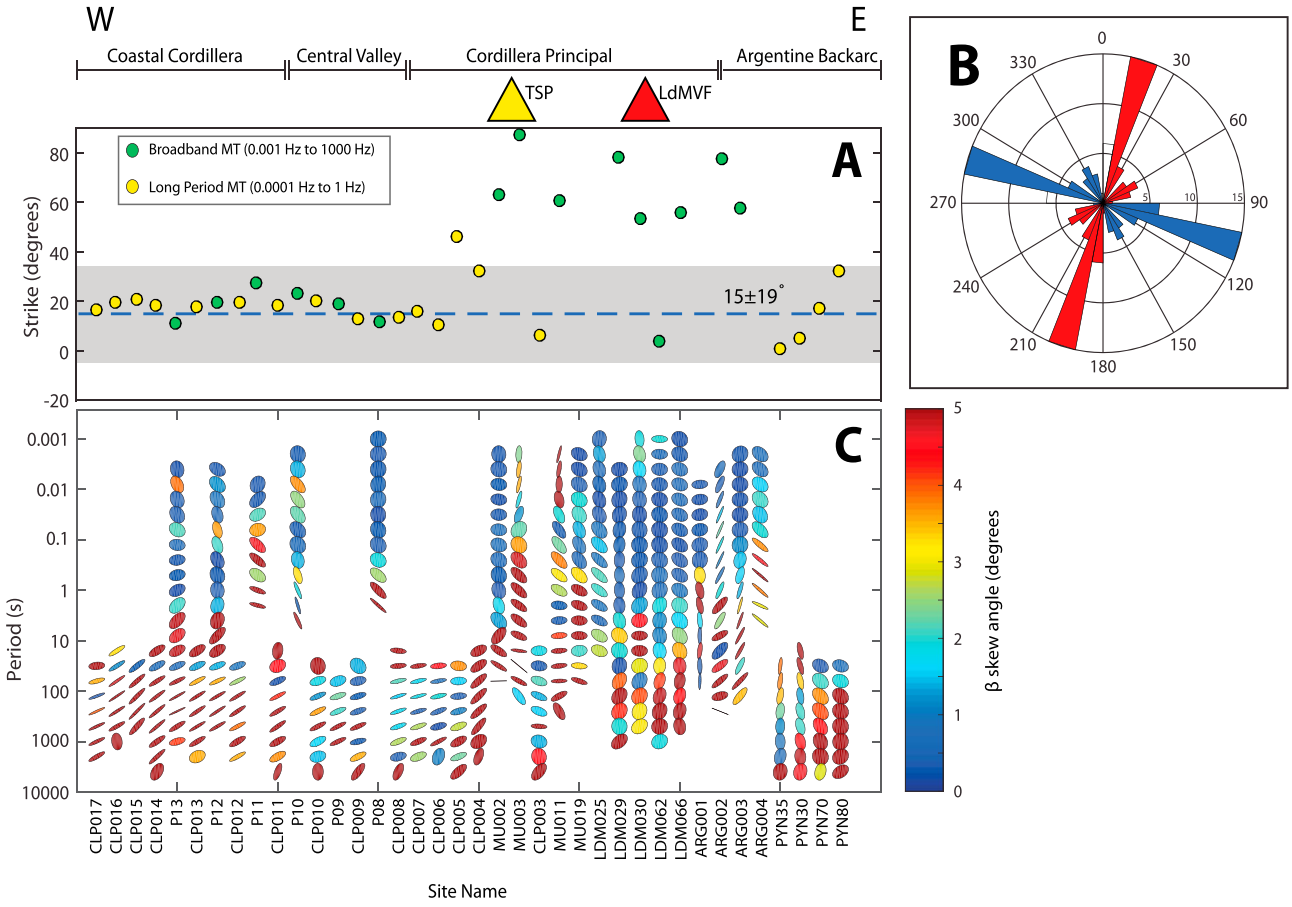

Figure 2. Dimensionality and directionality analysis for MT data. (a) The strike for each station along the profile as determined from tensor decomposition (McNeice & Jones, 2001). The average strike (15°) is plotted as blue dashed line and the one circular standard deviation error bar is shown in the gray box, which encompasses all the stations except 9 anomalous stations with scattered strikes in the Cordillera Principal. Yellow dots are long-period sites, and green dots are broadband sites. (b) A rose diagram showing a circular histogram of strike values for all sites determined from tensor decomposition. The majority of sites lie within the 15° to 25° strike bin. A 90° ambiguity exists as shown by the red and blue parts of the histogram. (c) A phase tensor pseudosection shows the MT profile as a function of period. Each ellipse on the plot denotes the phase tensor for a single period at a single MT site. More elliptical phase tensors indicate more 2-D or 3-D structure, while circular phase tensors suggest 1-D geoelectric structure. Each phase tensor is colored by its β-skew angle where blue indicates relatively 1-D or 2-D, undistorted data and red indicates data with 3-D distortion. TSP = Tatara-San Pedro. LdMVF = Laguna del Maule Volcanic Field; MT = magnetotelluric. Note that distances along profiles are not to scale.

longer period sites on the eastern side of the profile (i.e., east of the Cordillera Principal). This has an impact on the inversions and necessitates a two-step procedure as detailed below. The apparent resistivity and phase data are shown for four sites, CLP016, P08, CLP008 and LDM029 in Figure 3. CLP016 is a long-period site located in the Coastal Cordillera and shows steeply decreasing TE mode apparent resistivity and steeply increasing TM mode apparent resistivity which is a typical coast effect. Further east, P08 is a broadband MT site and CLP008 is a long-period MT site. These sites are only 5 km apart and are combined to show how the broadband and long-period MT compare but were inverted as separate sites in the inversion. The match is quite good for the apparent resistivity although there is a mismatch in the phases between the bands, which may be due to poor data quality at shorter frequencies for the long-period data or different near-surface structure. It is worth noting that CLP008 lies in a valley, while P08 is on a flat section of the Central Valley. Finally, LDM029 is shown as a representative broadband MT site in the Cordillera Principal near the LdMVF and shows two-distinct minima in the apparent resistivity curve indicating the presence of shallower and deeper conductors.

Vertical magnetic field data were collected at all sites except two broadband locations. This additional field component allowed for the computation of vertical magnetic transfer functions (i.e., the ratio of the vertical component to the horizontal component). Induction vectors (IVs) show the vector sum of the two vertical

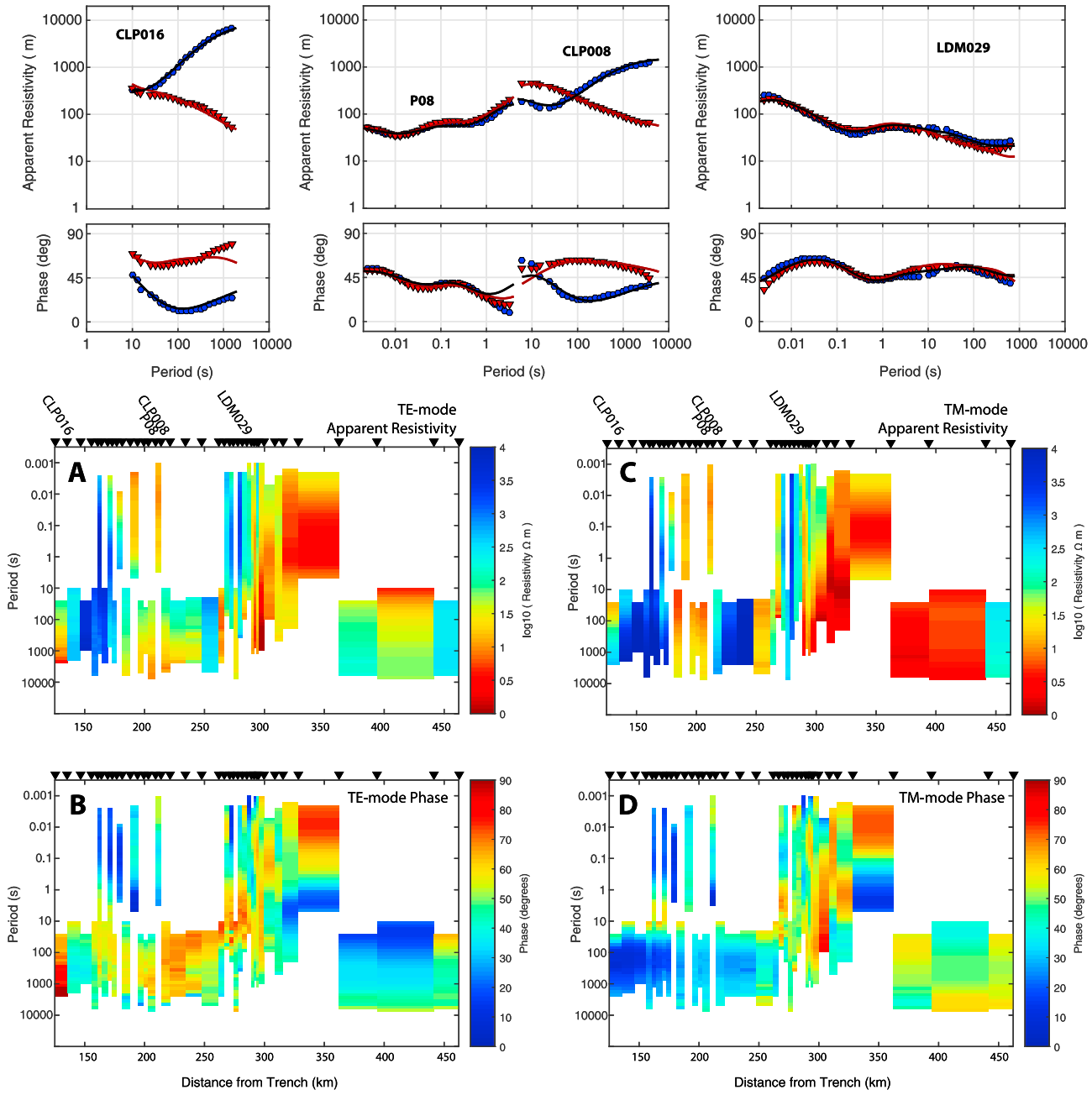

Figure 3. Magnetotelluric (MT) data and pseudosections. The top three panels show apparent resistivity and phase data for four MT sites in the Coastal Cordillera (CLP016), Central Valley (P08, CLP008), and Cordillera Principal (LDM029). Transverse electric (TE) mode is shown as red triangles, while transverse magnetic (TM) mode is shown as blue circles. Inversion model fit is shown as solid lines. Sites CLP016 and CLP008 are both long period, whereas P08 and LDM029 are broadband. Sites P08 and CLP008 are located less than 5 km apart and are shown on the same plot but were treated as separate sites in the inversion. Below are pseudosection plots showing (a) TE mode apparent resistivity, (b) TE mode phase, (c) TM mode apparent resistivity, and (d) TM mode phase for each site along the profile as a function of period. Red colors denote low apparent resistivity and high phase (i.e., decreasing resistivity), while blue denotes high apparent resistivity and low phases (i.e., increasing resistivity). All data have been rotated to $x = 15°$ east of north and $y = 105°$ east of north. TE mode is calculated with x oriented electric fields and y oriented magnetic field, whereas TM mode is the orthogonal case.

magnetic transfer function real components. In map view, the vectors can be plotted as arrows, which point away from conductors (Wiese, 1962) where the length of the arrow indicates the magnitude of the vector sum as shown in Figures 4a and 4b at periods of 50 and 2,000 s, respectively. Sites in the Coastal Cordillera show large IVs (i.e., long arrows), which point away from the Pacific Ocean likely indicating the large ocean effect at short periods. However, at sites in the Central Valley and the Cordillera

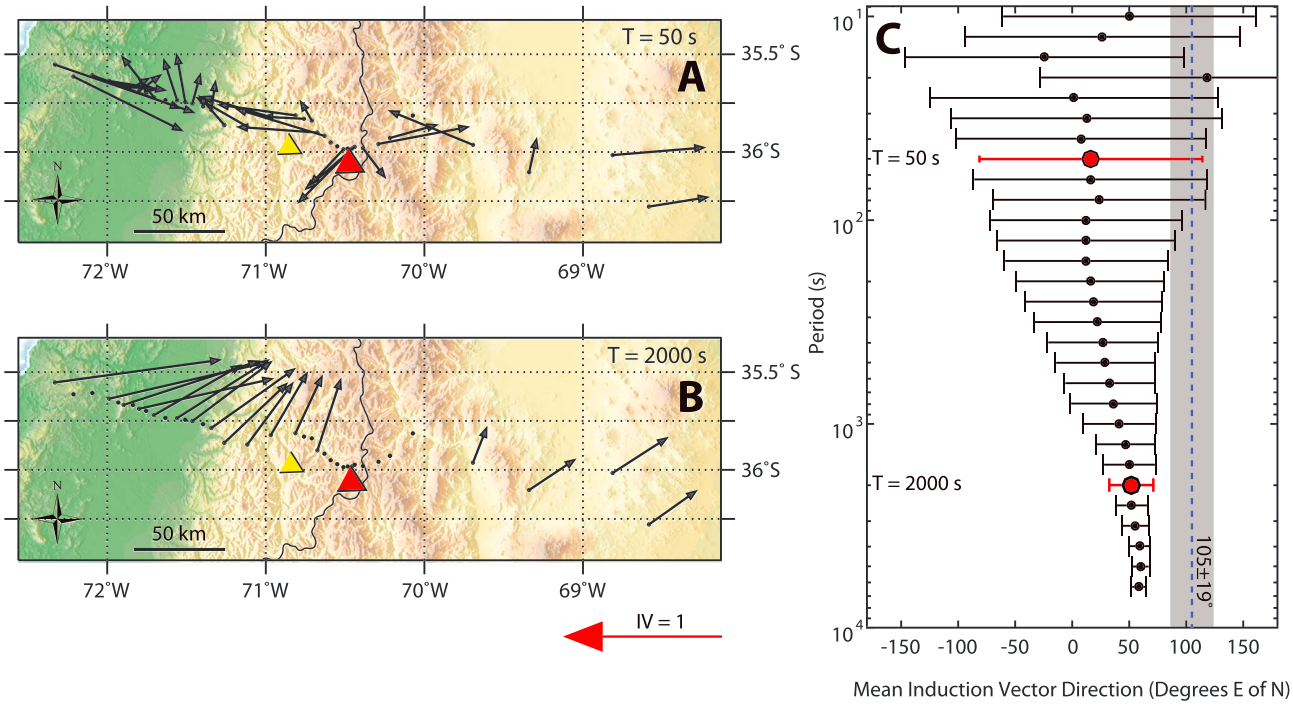

Figure 4. A comparison of induction vectors (IVs) and tensor decomposition strike. IVs should be perpendicular to strike (see text for more details) and point away from conductors in the Weise convention. (a) A map of IVs at 50-s period. Large scatter shows no consistent trend in IV direction. (b) A map of IVs at 2,000-s period. Here, IVs consistently point toward the northeast. Red triangle = Laguna del Maule volcanic field. Yellow triangle = Tatara-San Pedro volcano. (c) A plot of mean IV direction as a function of period. At short periods (i.e., shallower depths), error bars are large, indicating scattered induction angles. At longer periods (i.e., deeper depths), error bars are small with a mean direction of approximately N50°E. The blue dashed line shows the mean profile direction perpendicular to geoelectric strike (gray box denotes one standard deviation). In a perfect 2-D case, IV direction and profile direction should be the same. Note that periods less than 10 s are not plotted because IVs are very scattered at shallow depth.

Principal, the IVs are very scattered at short periods. All the IVs surrounding the LdMVF point away from one another, suggesting a conductor at depth beneath the LdMVF. At greater depths (i.e., longer periods; Figure 4b), IVs are very consistent in pointing toward the northeast at all sites along the profile, which have long-period data. This suggests a regional structure at depth. However, under a 2-D isotropic assumption, it is expected that IVs will be perpendicular to the geoelectric strike since all conductors will be aligned orthogonal to the geoelectric strike. Figure 4c shows that this is not the case. Using directional statistics, the mean and standard deviation of the IV direction was calculated at each period and is plotted as a function of period. It can be seen that the scatter in the IVs is very large at short periods but at longer periods, the error bars are much smaller indicating a much more consistent direction. More importantly, the direction of the IVs is approximately N50°E, which is not perpendicular to the geoelectric strike as a determined by tensor decomposition. In an ideal 2-D scenario, it would be expected that the IVs would all point at N105°E ± 19° (the gray box in Figure 4c). This further suggests that the ideal 2-D, isotropic assumption is being violated. Brasse et al. (2009) found a similar phenomenon in the southern Andes (38–41°S) where IVs also pointed uniformly to the northeast at periods greater than 3,000 s. They showed that this discrepancy could be accounted for with an anisotropic layer in the overriding South American plate, which they attributed to a fractured and fluid-rich lower crust.

With these considerations in mind, a 2-D isotropic inversion was carried out with the understanding that results may be more robust on the west side of the profile where the strike is better defined and that electrical anisotropy may be a factor in parts of the lower crust. Future anisotropic inversions would further elucidate the effects of anisotropy in this region of Chile. The impedance data were rotated to N15°E, representing the best fitting regional strike, and impedance data were inverted to find the best fitting model using the non-linear conjugate gradient method of Rodi and Mackie (2001). The ocean was included with a fixed resistivity of 0.3 Ωm using local bathymetry. Inverting without static shifts resulted in high data misfit values, and it was necessary to include static shifts in all inversions. The data set used in the inversion included 38 sites

with 2,590 complex impedance data points over a period range of 0.001 to 10,000 s. The data set included 19 long-period sites with periods from 10 to 10,000 s and 19 broadband sites with periods from 0.001 to 1,000 s. Sites were projected onto a N105°E profile with interpolated topography. Both the TE and TM mode were inverted. Since the TE mode was consistently noisier than the TM mode, an error floor of 10% was applied to the TE mode and 5% to the TM mode. This choice of error floor effectively downweights the importance of the noisier TE mode data in the inversion. The 100-Ωm starting model had 97 vertical cells beginning with 50-m-thick topography cells and growing geometrically downward to a maximum thickness of 73.9 km. The maximum depth of the model was 450 km below surface. The model included 86 horizontal cells with variable width based on station spacing with a mean value of 3.5 km. The model also included 12 horizontal padding cells in each direction growing geometrically to 750 km from the center with maximum cell thickness of 217 km.

A variety of possible inversion methodologies and options were investigated in an effort to create the most plausible resistivity model. In one variation, a smoothing constraint was placed on the model at the top and bottom of the Nazca plate using the Slab 1.0 model of Hayes et al. (2012) and an estimated plate thickness of 50 km (Sodoudi et al., 2011). In another variation, no smoothing constraint was applied. The regularization parameter (τ) was varied to produce an L-curve, which optimized the trade-off between model smoothness and data misfit. The optimal smoothing parameter was $\tau = 2$ for both constrained and unconstrained inversions and the L-curve for the constrained case is shown in supporting information Figure S2. A third variation removed high skew impedance data ($\beta > 6°$) and inverted only the low skew data (supporting information Figure S3). This decreased the amount of data available and thus decreased resolution but provided a more 2-D approximation. A final variation which was ultimately used as the preferred inversion model involved inverting only the long periods (>10 s) and used the resulting inversion model as the starting model for a second inversion with all periods. This two-step methodology proved an effective means of giving greater weight to the long-period data (which have a more well-defined geoelectric strike) while still resolving shallow structure. A variety of models with different data and smoothing parameters are shown in supporting information Figure S4. In general, the primary conductive and resistive features are robust and independent of modeling methodology.

3. Inversion Results and Interpretation

3.1. Model Interpretation

The preferred constrained and unconstrained inversion models are shown in Figure 5 along with the location of the slab from Hayes et al. (2012) and the location of the Moho from Laske et al. (2013). Deep earthquake epicenters (>50 km) are from IRIS Data Services (2018), while shallow earthquake epicenters (<50 km) are taken from an improved database from Hicks et al. (2014) using aftershocks from the 2010 Maule earthquake (see supporting information Figure S5). Earthquakes within 50 km of the profile are projected onto the profile. The preferred resistivity models used the two-step methodology and the starting model for each inversion is shown in supporting information Figure S4. The constrained and unconstrained inversions have root-mean-square (r.m.s) data misfit values after 200 iterations of 1.51 and 1.54, respectively. Figure 5c shows the r.m.s. misfit for each station for both constrained and unconstrained inversions as well as the static shift parameters for the constrained case. The r.m.s. misfit is similar for both inversions and shows higher misfit near the volcanic arc as expected due to scattered geoelectric strike directions observed in that area. Because MT inversions are nonunique, it is preferable to include the a priori information of the slab interface to the model, which will result in more geologically consistent models with fewer unknowns (Pommier & Evans, 2017). This is further shown with a variety of inversion tests (supporting information Figure S4) and using a synthetic experiment (supporting information Figure S6) whereby an unconstrained and constrained model are compared to a known "true" model. As such, the constrained inversion will be interpreted throughout this paper. For this particular profile, it seems that whether the slab constraint is imposed or not has little effect on the shallow conductive features because most features are the same in both models in Figure 5. However, at depth, the imposition of the slab boundary constraint tends to smooth down features toward the slab interface. Because the inversion uses an irregular combination of both long-period and broadband MT sites, it is important to be aware of the relative sensitivity of the model. A relative sensitivity map calculated from the Jacobian is shown in supporting information Figure S7 (Mackie & Madden, 1993; Rodi & Mackie, 2001). In general, resolution is good above 100 km although, due to the lack of long-

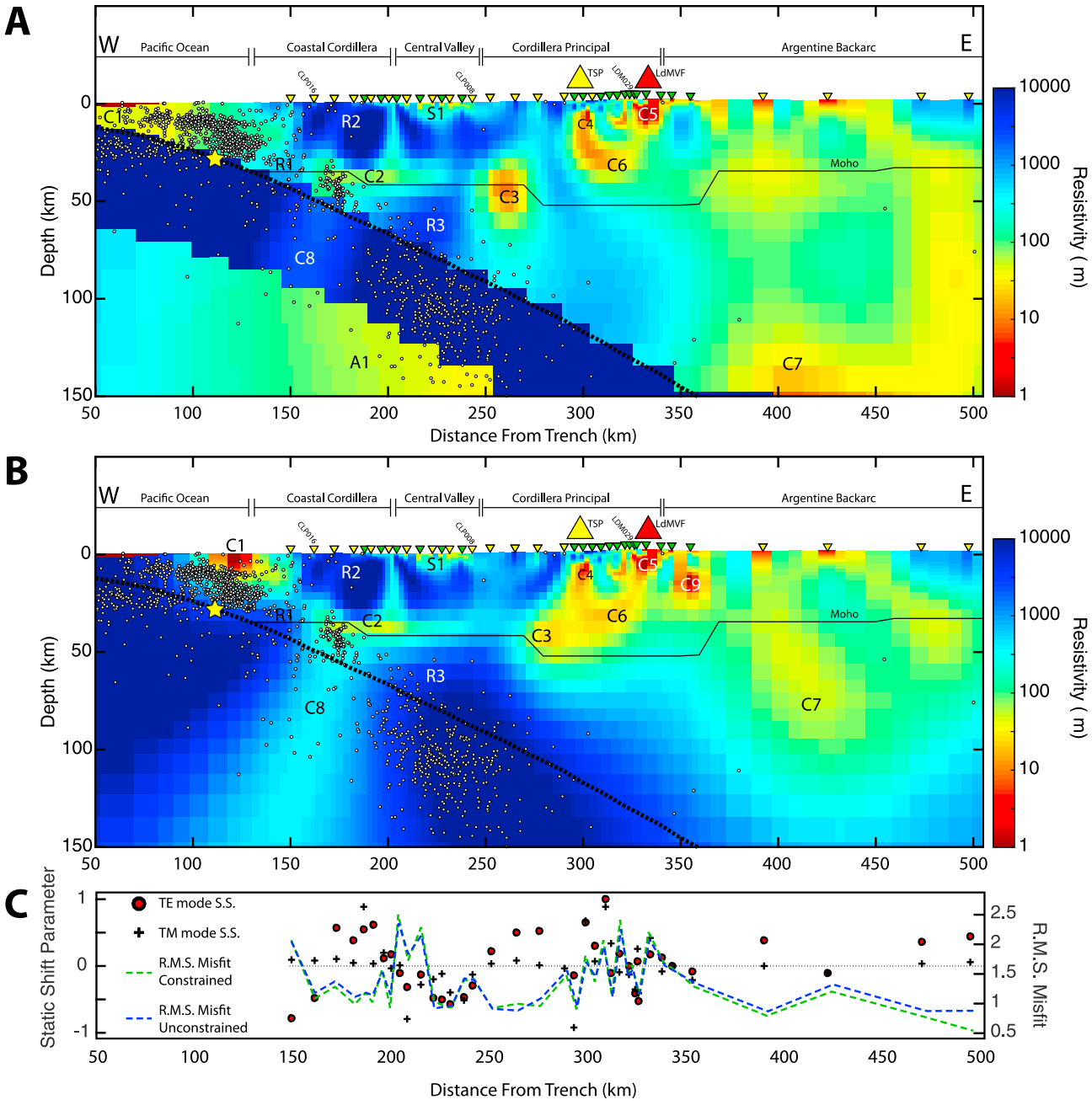

Figure 5. The preferred 2-D inversion model along the magnetotelluric (MT) profile for both the slab constrained (a) and unconstrained (b) cases. Broadband MT sites are shown as green inverted triangles, and long-period MT sites are shown as yellow inverted triangles on the surface of the model. Conductors are labeled C1 through C8, and resistors are labeled R1 through R3. The shallow surface conductor in the Central Valley is labeled S1, and deeper slab-side conductor is labeled A1. The location of the subducting slab is taken from Hayes et al. (2012) and shown as a thick black dashed line. This is the location of the tear which constrained the inversion to have zero smoothing across the boundary. The Moho discontinuity, shown as a thin black line, is taken from the Crust1.0 model of Laske et al. (2013). The location of the 2010 Maule earthquake is shown as a yellow star. Earthquake epicenters are shown as small white dots. TSP = Tatara-San Pedro. LdMVF = Laguna del Maule Volcanic Field. The lower panel (c) shows root-mean-square (r.m.s.) misfit for both constrained and unconstrained cases for each station along profile. It also shows the static shift parameters applied to the constrained inversion.

period sites near the volcanic arc and overlying conductors, resolution is poorer at depth beneath the volcanic arc.

All apparent resistivity and phase data fit curves for the constrained and unconstrained inversions are shown in supporting information Figure S1 and the inversion data fit is shown for sites CLP016, P08, CLP008, and

LDM029 in Figure 3. Pseudosections of observed and inverted data and residuals are shown in supporting information Figure S8.

There are seven primary conductive features present in both models in Figure 5 and several significant resistive features, all of which were investigated using sensitivity tests. At the surface, a conductor (S1) coincides with the volcaniclastic sedimentary fill of the Central Valley (Reyes-Wagner et al., 2017). Feature C1 is a conductor (<10 Ωm) located at shallow depth (<15 km) beneath the trench. This conductor is poorly resolved with the current data set and would require offshore MT data to improve the resolution of this feature (Evans et al., 2002). The difference in shape and resistivity of this feature in the constrained and unconstrained inversions highlights this insensitivity. However, a strong conductor in the accretionary wedge is expected and would likely be due to early dehydration as pore-bound fluids are expelled from the downgoing slab at shallow depths via compaction and lithification (Hyndman et al., 1997). Additionally, conductivity could be enhanced by a preponderance of clay-rich minerals (e.g., smectite), which provide additional pathways for electrical current to flow along the surface of mineral grains (Hyndman et al., 1997; Pommier & Evans, 2017).

In the constrained inversion, the slab interface beneath the MT profile is not characterized by a continuous conductive zone along the interface but instead shows a sequence of resistive and conductive features as the slab descends from the surface to a depth of 150 km (Figure 5a; C1, R1, C2, R3, C3, and C7). This sequence of conductors suggests discrete locations and depths where fluids are released in large quantities and are able to migrate into the overlying crust or mantle. This stepwise continuous dehydration has been supported by numerical studies (e.g., Schmidt & Poli, 1998; van Keken et al., 2011) and is in contrast to single phase dehydration models in which dehydration occurs at a single depth. This segmentation of conductors has also been reported in other MT images of subduction zones (e.g., Jödicke et al., 2006; McGary et al., 2014; Soyer & Unsworth, 2006; Wannamaker et al., 2014). On the edge of the MT profile at 150 km east of the trench a resistor (R1) is located at 25-km depth. East of R1, between 150 and 200 km east of the trench, a weaker conductor (C2; 30 to 50 Ωm) is located at 25- to 30-km depth beneath the highly resistive (>10,000 Ωm) Paleozoic accretionary complexes of the coastal ranges (R2; Hervé et al., 2013). The depth to C2 is consistent in both the constrained and unconstrained inversion and is notably more than 15 km above the slab interface and is in a similar location as anomalies found in MT studies in southern Chile (Brasse et al., 2009). C2 also spreads out laterally eastward, extending parallel to the Moho. This conductor is likely the result of fluids released from prograde metamorphism of clay-rich oceanic upper crustal sediments as they transition to the blueschist facies (Hensen et al., 2004; Peacock, 1990; Völker & Stipp, 2015). The fact that this conductor is located approximately 10 km above the slab interface may suggest that this region is more permeable and/or faulted, which allows dehydrating fluids to migrate upward into the overriding crust before being trapped beneath the less permeable Paleozoic block (R2). It is also important to note that the slab itself is approximately an order of magnitude more conductive (C8) directly beneath C2, and C8 correlates with the transition from interplate to intraslab seismicity. This feature is also more pronounced in the unconstrained inversion (Figure 3b) and becomes even more prominent at low τ values (see supporting information Figure S2).

Continuing to the east is a resistive block (R3, >1,000 Ωm) at approximately 60-km depth and 225 km from the trench. This could be a resistive block of mantle with a low fluid content and suggests that there are minimal dehydration reactions occurring along the slab at this location. At 250 km from the trench and at 40-km depth, is a prominent conductor (C3, <10 Ωm), which straddles the continental Moho. This conductor is located approximately 30 to 40 km west of the modern volcanic arc. When the slab constraint is imposed (Figure 5a), the area at the slab interface beneath C3 is an order of magnitude more conductive than R3. When the slab constraint is not included (Figure 5b), C3 is weaker and smoothed eastward and appears connected to other conductors beneath the volcanic arc. The two inversions neither confirm nor refute the idea that there is a geological connection. It is interesting to note that the inversion which excludes the high skew data (supporting information Figure S3) also images C3 with greater connection to the volcanic arc so it appears that the precise position of C3 is not well constrained. A denser MT data array is needed in this area to provide greater constraints in this part of the model. This conductor likely signifies an important dehydration event at a depth of approximately 80 to 90 km along the slab interface related to the breakdown of amphibole and the transition to the eclogite facies, which releases fluids into the overlying mantle (Hacker, 2008; Poli & Schmidt, 1995; van Keken et al., 2011). This assumes vertical fluid transport although, depending on the properties of the mantle, it is possible that C3 is a result of fluid focusing from fluids

derived from a wide range of depths (Wada & Behn, 2015; Wilson et al., 2014). A mantle wedge conductor similar to C3 has been imaged at similar depths in subduction zones around the world (see Worzewski et al., 2011, and references therein). However, in the sample of Worzewski et al. (2011), the anomaly in south Chile from Brasse et al. (2009) is a notable outlier, being >60 km west of the volcanic arc. As seen in Figure 5a, C3 is only 40 km west of the volcanic arc which is more in line with the global average (Worzewski et al., 2011). This suggests some significant along-strike variation in mantle wedge structure between south Chile and central Chile, which may be linked to the thermal structure of the downgoing slab. The Nazca plate in south Chile is younger and hotter, which may lead to basalt-eclogite dehydration at shallower depths than central Chile. This is supported by numerical modeling by Völker and Stipp (2015) who showed that a significant dehydration event occurs approximately 50 km west of the volcanic arc for the Maule region but occurs further west when the Nazca plate is younger (i.e., in south Chile). This is also supported by earlier numerical work showing that intermediate temperature slabs release more water earlier (i.e., shallower) than low-temperature slabs (e.g., Kerrick & Connolly, 2001). Forearc fluids trapped in the lower crust and upper mantle (C2 and C3) may account for some of the missing fluids which are not accounted for when calculating volcanic H_2O output and deep slab water sequestration (Worzewski et al., 2011).

Directly beneath the volcanic arc, there are three crustal conductors present in both models (Figure 5). A large conductor (C4) directly beneath TSP at shallow depth (<10 km) likely represents a zone of partial melt associated with this recently active system and responsible for heat and hydrothermal fluids as identified by recent geothermal exploration projects (Hickson et al., 2011). To the east, beneath the rear-arc LdMVF, a large conductor (C5) stretches over a large region 325 to 350 km east of the trench at shallow depth (<10 km). This likely represents a poorly resolved portion of the highly three-dimensional LdMVF magmatic system as detailed by Cordell et al. (2018). Below both TSP and the LdMVF, there is a large conductor (C6) at intermediate depths of 25 to 40 km. This is likely a lower crustal MASH zone (Hildreth & Moorbath, 1988) where mafic melts rising due to buoyancy from the subducting slab stall at the crust-mantle density boundary. Here, melts differentiate and assimilate crustal components and become more felsic before rising further into the crust as more andesitic-to-silicic melts (Ducea et al., 2015). It appears that C6 could be a lower crustal zone which feeds melts to both TSP and the LdMVF from a common source. Petrological analyses at both complexes show similar isotopic compositions and both suggest lower crustal assimilation (Andersen et al., 2017; Davidson et al., 1987). In the unconstrained inversion, another conductor (C9) is also present to the east of LdMVF at shallow depth (<15 km); however, this feature is rarely present in other inversions (see supporting information Figures S2–S4) and seems to be an artifact of the long-period inversion which struggles to resolve shallow structure.

The final deep features in the model are the conductive backarc, specifically a deep conductor at >130-km depth (C7) and the conductive subslab asthenosphere (A1). Due to the sparse MT station spacing in Argentina, any conductive anomalies in the backarc are poorly resolved and on the edge of the profile. However, it is clear that the entire backarc is quite conductive, which is in agreement with the three-dimensional MT analysis of the Payún Matrú complex and surrounding area made by Burd et al. (2014) in which they identified the Shallow Western Asthenospheric Plume approximately 100 km east of the LdMVF. C7 may be a poorly resolved 2-D version of the 3-D Shallow Western Asthenospheric Plume feature and may be due to fluid and partial melting related to de-serpentinization of the slab and high temperatures at depth (Völker & Stipp, 2015). Numerical modeling by Völker and Stipp (2015) suggest that a large amount of downgoing fluids (e.g., >80%) remains in the subducting slab into the backarc in the Maule region. This value is greater than in southern Chile and significantly greater than in other younger subduction zones such as Cascadia (van Keken et al., 2011). This could explain why the backarc conductor, C7, is so much larger than the forearc conductors and farther east than similar conductors in Cascadia (e.g., Wannamaker et al., 2014). The Nazca subslab asthenosphere (A1) is only present when the slab is imposed but, with a value between 10 and 100 Ωm, can be explained by a small amount of partial melt and/or hydrated mantle (Bishop et al., 2017; Worzewski et al., 2011).

It is also interesting to note that no deep conductive features are imaged on the slab interface or in the mantle wedge directly beneath the volcanic arc. This may partly be due to model resolution as (a) only a few long-period MT stations were collected near the LdMVF and (b) the overlying conductors (C4, C5, and C6) will attenuate EM signals and limit model resolution at depth. For example, a conductor of similar size and

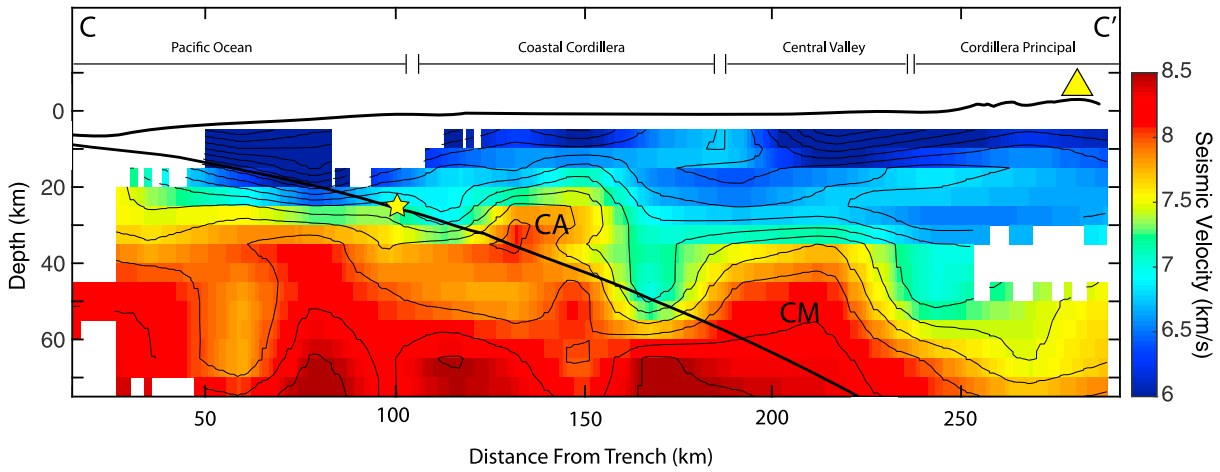

Figure 6. The *P* wave velocity seismic tomography model of Hicks et al. (2014) along profile C–C′ approximately 75 km south of the current magnetotelluric profile (see Figure 1 map). The yellow star denotes the location of the 2010 Maule earthquake. CA = Cobquecura anomaly. CM = continental mantle. The yellow triangle denotes the volcanic arc.

resistivity as C3 could exist at the slab interface beneath the volcanic arc and would not be detected with the current MT profile (see supporting information Figure S9). However, fluid release prior to the amphibole stability (i.e., <75 km) is generally much greater in volume than at pressures higher than amphibole stability (e.g., >75 km), and thus, high conductivity fluids may be less prevalent at the slab interface 300 km east of the trench (Schmidt & Poli, 1998; van Keken et al., 2011). Furthermore, the conductive backarc (C7) as shown in Figure 5 and by Burd et al. (2014) suggests the possibility that partial melting and deserpentinization occurs deeper and further east than younger subduction to the south.

3.2. Correlations With Previous Seismic Tomography

In previous 3-D seismic tomography studies, Hicks et al. (2012, 2014) imaged an undulating high-velocity structure along the plate interface between 100 and 200 km east of the trench (features CA and CM in Figure 6). This structure is similar to the sequence of conductors and resistors imaged in the forearc of the constrained MT model (Figure 5a). A comparison between the MT model and seismic model is shown in Figure 7. A slice was taken through the seismic velocity tomography model of Hicks et al. (2014) at the same location as the 2-D MT profile. Both the MT model and seismic model were interpolated onto the coarser seismic tomography grid with 10-km by 2.5-km cells to allow for direct comparison (Figures 7a and 7b). Note that the seismic model does not extend as far east and as deep as the MT model, so some of the structures near the LdMVF and the Argentine backarc are excluded from this analysis. The comparison also excludes the upper 5 km because the MT model included topography, while the seismic model did not and because the broadband MT model samples relatively small, heterogeneous structures in the near surface while the seismic velocity model is poorly constrained in the near-surface due to a lack of very shallow sources. A correlation histogram is shown for the shared model space (Figure 7d). The shared model space has a positive Pearson correlation coefficient of 0.32 indicating a weak linear correlation where higher velocities correlate with higher resistivities. This is expected since cold, dry rocks have high velocities and high resistivities while warm, wet rocks have low velocities and low resistivities.

The correlations are broadly grouped into four zones: (1) low velocity and low resistivity, (2) high velocity and high resistivity, (3) low velocity and high resistivity, and (4) high velocity and low resistivity (Figure 7c). A high resistivity is defined as any model cell greater than 100 Ωm (i.e., resistive deviations from the starting half-space) and similarly low resistivity is assigned to any model cell less than 100 Ωm (i.e., conductive deviations from the starting half-space). A low velocity is defined as any model cell with less than 7 km/s, and high velocity is any model cell with greater than 7 km/s using the terminology of Hicks et al. (2014). The conductors C1 and C2 both are in Zone 1 indicating both low seismic velocity and resistivity, which can be interpreted as a region of fluids. A low *Vp* (<5.5 km/s) and high *Vp*/*Vs* ratio (>1.8) has been identified in the same area as C1 giving additional evidence for a high fluid content due to overpressured

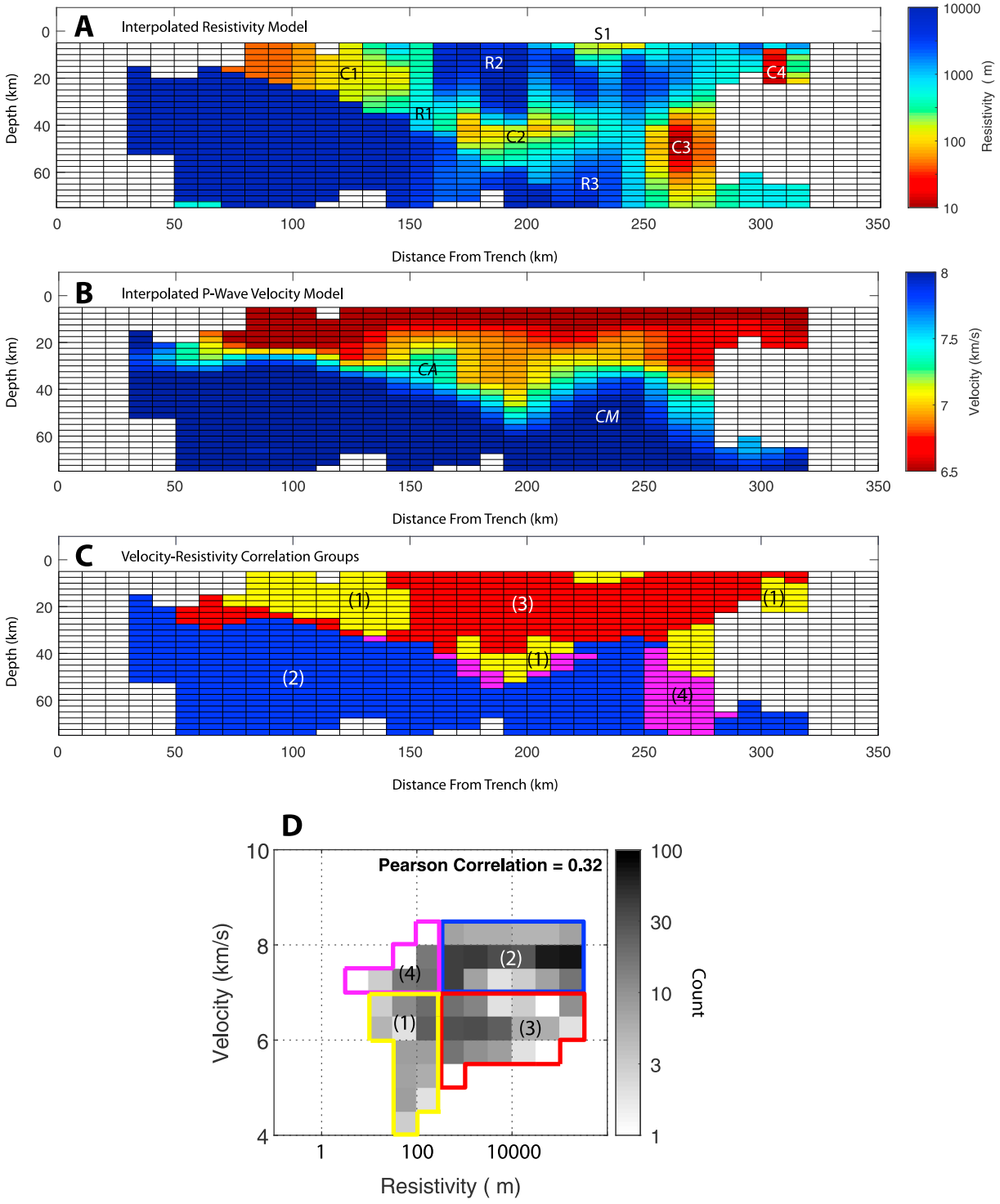

Figure 7. A comparison between the 3-D seismic tomography model of Hicks et al. (2014; see Figure 6) and the constrained magnetotelluric (MT) model (see Figure 5a). Both models have been interpolated onto a common mesh. (a) The MT model showing resistivity along the profile as a function of depth with labels matching the features shown in Figure 5. (b) A 2-D slice through the 3-D seismic model of Hicks et al. (2014) along the same profile as the MT model. Red denotes low velocity, while blue denotes high velocity. This is the opposite color scale as shown in Hicks et al. (2014), but it is done to allow direct color comparison between the MT and seismic models. Labels denote CA (Cobquecura anomaly) and CM (continental mantle) from Hicks et al. (2014). (c) The shared model space mapped into four categories of velocity and resistivity correlations. (d) A correlation histogram showing the number of model cells, which share each velocity-resistivity pair. The color of each square denotes the number of model cells on a logarithmic scale. Much of the model space has a resistivity of approximately 25,000 Ωm and a velocity of approximately 8.5 km/s. This denotes the high-velocity and high-resistivity zones of the subducting slab. The overall Pearson correlation between the models is 0.32 indicating a weak correlation.

sediments at shallow depth near the trench (Hicks et al., 2014). Despite the fact that C1 is on the edge of the MT profile, the good correlation between the seismic and MT models at this location suggests that it may be a real structure linked to expulsion of fluids from pore spaces. The conductor C2 also correlates with a low-velocity zone from Hicks et al. (2014). Hicks et al. (2014) did not specifically interpret this low-velocity zone but, with the addition of MT, it seems that this low *Vp* and high *Vp*/*Vs* ratio zone may correspond to dehydration-related fluids and/or a serpentinized mantle. This zone is also associated with high afterslip following the Maule 2010 earthquake as evidenced by a cluster of aftershocks (Hicks et al., 2014; Rietbrock et al., 2012) and large aseismic afterslip (Lin et al., 2013), which also indicates fluid-driven processes. Farther east, toward the edge of the seismic model, Zone 1 also correlates with the top of the C3 conductor just west of the volcanic arc. Unfortunately, the seismic model does not extend east to the LdMVF or backarc to provide additional constraints to the structures along the volcanic arc. C4 is on the edge of the tomography model and does lie in Zone 1, but it is not necessarily evidence of a seismic anomaly related to the LdMVF volcanic system. More recent work using ambient noise tomography indicates there is a low Vs anomaly beneath the LdMVF between 3- and 8-km depths (Wespestad et al., 2019).

The resistive downgoing slab correlates with Zone 2 indicating relatively dry, cold, and impermeable mafics and ultramafics. The shallow structure (i.e., <20-km depth) east of the Pacific Ocean is within Zone 3 and is broadly low velocity and simultaneously higher resistivity (e.g., R2). This may be due to smearing in the tomography model as the frequency bandwidth for tomography studies does not allow for detailed study of near-surface structures. The resistor R1 coincides with the high-velocity Cobquecura anomaly (CA), which was initially interpreted as an ancient seamount on the subducting slab (Hicks et al., 2012) and was also noted as a density high in the gravity survey of Maksymowicz et al. (2015). Further geological interpretation and additional seismic data suggest that it is more likely to be a dense block of peridotite above the modern slab, which fed Triassic intrusions into the Coastal Cordillera when it was an ancient volcanic arc (Hicks et al., 2014). The interpretation of this feature as a cold block of unaltered and relatively impermeable peridotite is supported by the MT model, which shows a resistor (R1) in that location. The center of the Cobquecura anomaly in the 3-D seismic tomography model is approximately 75 km south of the MT profile and thus the resistivity model may only be imaging the northern edge of this resistive block. The resistor R3 aligns with feature CM in Hicks et al. (2014) and is likely the eastward limit of the nonconvecting mantle wedge.

Zone 4 shows high velocities and low resistivities and correlates with the base of conductor C3. This is somewhat surprising as the depth aligns with the expected release of large volumes of fluid as downgoing rocks transition to the eclogite facies and as such one would expect a slower velocity structure. This anomalous correlation is most likely explained by the fact that it is on the edge of the seismic tomography model where there is limited resolution to the east at depth. However, a geological explanation is also possible because the basalt-eclogite transition is accompanied by an increase in velocity in the downgoing slab due to an increase in density (Pommier & Evans, 2017).

3.3. Correlations With Observed Seismicity

The seismicity of the region can be grouped broadly into two primary clusters. The first cluster is a group of shallow focus earthquakes at depths less than 25 km and west of the Chilean coast (Figure 5). This seismogenic zone is prone to brittle fracture and stress accumulation which leads to large megathrust earthquakes such as the 2010 Maule earthquake (Hicks et al., 2012; Moscoso et al., 2011). This cluster overlaps with C1, which is interpreted as early fluid release. Moreno et al. (2014) showed that regions of high fluid content are associated with higher pore pressure, which leads to aseismic slip behavior. A dense offshore 3-D MT survey would be needed to probe any 3-D heterogeneity in the structure of C1 as was found in New Zealand (Heise et al., 2017).

The second cluster of earthquakes is at intermediate depths of 75- to 100-km depth approximately 200 to 250 km east of the trench (Figure 5). This second cluster is located almost entirely within the resistive downgoing slab and underlies both R3 and C3. These intraslab earthquakes are likely driven by dehydration embrittlement as fluids are released (Hacker et al., 2003). The fact that no conductor is imaged at the same location as these intraslab earthquakes suggests that the fluids in the slab occupy relatively small, disconnected pore spaces that go undetected by the MT data. Fluid focusing effects may play a role in collecting these fluids into a connected zone which is imaged as the forearc mantle wedge conductor (C3).

Between these two clusters of earthquakes are some additional correlations. The resistor R1 has almost no seismicity associated with it. This further suggests that R1 is an anomalous hard, strong asperity on the plate interface that defines the downdip coseismic rupture limit of the Maule earthquake (Hicks et al., 2014; Moreno et al., 2012). There is a small cluster of earthquakes associated with C2 directly above C8 (Figure 5). The seismicity in this cluster occurred following the 2010 Maule earthquake, and prior to that, there was relatively little known seismicity here in the interseismic period. This suggests that most stress is accommodated via aseismic slip, which is consistent with the Maule afterslip model of Lin et al. (2013). Fluids released from the slab (C2 and C8) may lead to serpentinization of the forearc mantle which is associated with stable sliding and often defines the downdip limit of the seismogenic zone (Hyndman et al., 1997; Hyndman & Peacock, 2003). This is further supported by a relatively high Vp/Vs ratio (~1.85) in this region (Hicks et al., 2014). The fact that some earthquakes did occur in C2 following the 2010 Maule earthquake suggests that fluid-driven diffusion stress processes may be important here and that this region may be a transitional zone of conditional stability that becomes unstable during or following transient high strain events (Lay et al., 2012). Dehydration at C2 and C8 may also induce microseismic events (<2.5 magnitude) that are not detected in the earthquake database of Hicks et al. (2014). The MT results suggest that fluid release and serpentinization of the forearc mantle may be an important control on aseismic zones, whereas relatively fluid-poor regions (e.g., R2) result in increased frictional plate-locking and more stick-slip behavior.

4. Conclusions

The electrical conductivity model presented in this paper allows us to investigate a range of subduction processes operating at different locations and at different spatial scales in the central Chilean subduction zone. The MT model is interpreted as revealing a comprehensive fluid and dehydration cycle from the forearc to the backarc including significant pore fluid expulsion (C1), blueschist facies dehydration and basalt-eclogite dehydration (C2 and C3), and deserpentinization at depth (C7). This suggests that fluid release does not necessarily occur as a single pulse but occurs in a punctuated stepwise continuous fashion at different depths during important mineral transitions as suggested by the numerical modeling of subduction zones (Schmidt & Poli, 1998; van Keken et al., 2011; Völker & Stipp, 2015). The position of the wedge conductor (C3) is similar to that found by other MT studies of subduction zones worldwide but is deeper and nearer to the volcanic arc than the conductor identified in south Chile by Brasse et al. (2009). This highlights the effect of along-strike variations in the thermal regime, fluid release, slab structure, and permeability as the Nazca plate is younger and hotter further south, which means the transition to eclogite may occur at a shallower depth (Völker & Stipp, 2015).

The volcanic arc beneath central Chile contains several important upper crustal (C4 and C5) and lower crustal (C6) conductors, likely representing local regions of melt accumulation. The conductor geometry raises the possibility that the arc volcanoes (e.g., TSP) and the rear-arc LdMVF share a common lower crustal zone of melt accumulation (C6), which may explain their similar isotopic signatures. As shown by Cordell et al. (2018), the electrical structure around the LdMVF is highly 3-D, and as such, conductor C5 is likely a 2-D approximation of the complex 3-D structure, which is not well imaged due to the coarser mesh used in this regional study.

As seen in other MT studies (see Pommier & Evans, 2017) the addition of the slab constraint in the MT model helps to image important structures on the plate interface and results in a resistivity model, which better aligns with previous seismic tomography studies and numerical studies. The resistive anomaly R1 coincides with a velocity high, which supports the interpretation of Hicks et al. (2014) that this region of the subduction zone has significant strong asperities of dense peridotite related to the ancient magmatic arc. These asperities may encourage plate locking and may help explain why large megathrust earthquakes, such as the 2010 Maule earthquake, initiate at this latitude as stresses concentrate at a strong structural contrast. The relatively aseismic zone between 40- and 60-km depths is likely related to slab dehydration (C2 and C8) and serpentinization of the forearc mantle, which leads to stable sliding and may be conditionally stable. Intermediate-depth earthquakes downdip of the aseismic zone do not appear to be correlated with any conductor, suggesting that fluids associated with dehydration embrittlement are relatively isolated and cannot

be imaged with MT. However, fluids released at depth migrate upward and become focused into a connected zone in the forearc mantle (C3).

IVs suggest a potentially anisotropic lower crust, similar to observations in southern Chile (40°S; Brasse et al., 2009). This highlights the need for future anisotropic inversions of this region. The generally three-dimensional data also highlight the need for a more comprehensive, 3-D MT array in this area of central Chile. An extension of the array to the south would be able to better image the Cobquecura anomaly while extension to the north would image the transition to the Pampean flat slab. Such an array would likely give even greater insight into along-arc variation in Chilean subduction zone structure.

Acknowledgments
This research has been supported by the National Science Foundation (grant number EAR-1411779) and the National Sciences and Engineering Research Council of Canada (NSERC) through a Discovery Grant to MJU and a PGS-D scholarship to D. C. We thank Catherine Hickson and Carolina Rodriguez for providing access to the MT data originally collected during exploration of the Mariposa Geothermal field by Alterra Power Corp (now Innergex Renewable Energy, Inc.). The MT data were collected in 2009 and 2010. Thank you to John Booker and Aurora Burd for providing long-period MT data from Argentina. Special thanks to Alan McNeice and Alan Jones for allowing us to use their strike tensor decomposition program. Wolfgang Soyer at CGG is thanked for reprocessing the broadband MT data. Special thanks to the Centro de Excelencia en Geotermia de Los Andes (FONDAP 15090013) and Universidad Católica de Chile for use of Metronix MT instruments. The facilities of IRIS Data Services, and specifically the IRIS Data Management Center, were used for access to earthquake epicenter locations plotted in this study. IRIS Data Services are funded through the Seismological Facilities for the Advancement of Geoscience and EarthScope (SAGE) Proposal of the National Science Foundation under Cooperative Agreement EAR-1261681. Ben Lee and Sean Bettac are thanked for discussions about the manuscript. Many individuals were involved with field work and other logistical support including Matthew Comeau, Ariel Figueroa, Jorge Gacitua, Renzo Mancini, Gustavo Pérez Guitiérrez, Brad Singer, Cliff Thurber, Gabriela and José Luis Valdés, and Nicolás Vera Cortés. Special thanks to Don Luis Torres for his invaluable knowledge of Laguna del Maule and his logistical support. MT EDI data files and the final constrained and unconstrained model files and input parameters are available at the PANGAEA data repository (https://doi.pangaea.de/10.1594/PANGAEA.899725). Lastly, we thank two anonymous reviewers for their useful comments, which greatly improved the manuscript.

References

Andersen, N. L., Singer, B. S., Jicha, B. R., Beard, B. L., Johnson, C. M., & Licciardi, J. M. (2017). Pleistocene to Holocene growth of a large upper crustal rhyolitic magma reservoir beneath the active Laguna del Maule Volcanic Field, central Chile. *Journal of Petrology*, *58*(1), 85–114. https://doi.org/10.1093/petrology/egx006

Angermann, D., Klotz, J., & Reigber, C. (1999). Space-geodetic estimation of the Nazca-South America Euler vector. *Earth and Planetary Science Letters*, *171*(3), 329–334. https://doi.org/10.1016/S0012-821X(99)00173-9

Bishop, B. T., Beck, S. L., Zandt, G., Wagner, L., Long, M., Antonijevic, S. K., et al. (2017). Causes and consequences of flat-slab subduction in southern Peru. *Geosphere*, *13*(5), 1392–1407. https://doi.org/10.1130/GES01440.1

Booker, J. R. (2014). The magnetotelluric phase tensor: A critical review. *Surveys in Geophysics*, *35*(1), 7–40. https://doi.org/10.1007/s10712-013-9234-2

Brasse, H., & Eydam, D. (2008). Electrical conductivity beneath the Bolivian Orocline and its relation to subduction processes at the South American continental margin. *Journal of Geophysical Research*, *113*, B07109. https://doi.org/10.1029/2007JB005142

Brasse, H., Kapinos, G., Li, Y., Mütschard, L., Soyer, W., & Eydam, D. (2009). Structural electrical anisotropy in the crust at the South-central Chilean continental margin as inferred from geomagnetic transfer functions. *Physics of the Earth and Planetary Interiors*, *173*(1-2), 7–16. https://doi.org/10.1016/j.pepi.2008.10.017

Burd, A. I., Booker, J. R., Mackie, R., Favetto, A., & Pomposiello, M. C. (2014). Three-dimensional electrical conductivity in the mantle beneath the Payún Matrú Volcanic Field in the Andean backarc of Argentina near 36.5°S: Evidence for decapitation of a mantle plume by resurgent upper mantle shear during slab steepening. *Geophysical Journal International*, *198*(2), 812–827. https://doi.org/10.1093/gji/ggu145

Caldwell, T. G., Bibby, H. M., & Brown, C. (2004). The magnetotelluric phase tensor. *Geophysical Journal International*, *158*(2), 457–469. https://doi.org/10.1111/j.1365-246X.2004.02281.x

Chave, A. D., & Jones, A. G. (2012). *The magnetotelluric method—Theory and practice*. Cambridge, UK: Cambridge Unviersity Press. https://doi.org/10.1017/CBO9781139020138

Cordell, D., Unsworth, M. J., & Díaz, D. (2018). Imaging the Laguna del Maule Volcanic Field, central Chile using magnetotellurics: Evidence for crustal melt regions laterally-offset from surface vents and lava flows. *Earth and Planetary Science Letters*, *488*, 168–180. https://doi.org/10.1016/j.epsl.2018.01.007

Davidson, J. P., Dungan, M. a., Ferguson, K. M., & Colucci, M. T. (1987). Crust-magma interactions and the evolution of arc magma: The San Pedro-Pellado volcanic complex, southern Chilean Andes. *Geology*, *15*(5), 443–446. https://doi.org/10.1130/0091-7613(1987)15<443:CIATEO>2.0.CO;2

Ducea, M. N., Saleeby, J. B., & Bergantz, G. (2015). The architecture, chemistry, and evolution of continental magmatic arcs. *Annual Review of Earth and Planetary Sciences*, *43*(1), 299–331. https://doi.org/10.1146/annurev-earth-060614-105049

Egbert, G. D., & Booker, J. R. (1986). Robust estimation of geomagnetic transfer-functions. *Geophysical Journal International*, *87*(1), 173–194. https://doi.org/10.1111/j.1365-246X.1986.tb04552.x

Evans, R. L., Chave, A. D., & Booker, J. R. (2002). On the importance of offshore data for magnetotelluric studies of ocean-continent subduction systems. *Geophysical Research Letters*, *29*(9), 1302. https://doi.org/10.1029/2001GL013960

Farías, M., Charrier, R., Carretier, S., Martinod, J., Fock, A., Campbell, D., et al. (2008). Late Miocene high and rapid surface uplift and its erosional response in the Andes of central Chile (33°–35°S). *Tectonics*, *27*, TC1005. https://doi.org/10.1029/2006TC002046

Feigl, K. L., Le Mevel, H., Tabrez Ali, S., Cordova, L., Andersen, N. L., DeMets, C., & Singer, B. S. (2013). Rapid uplift in Laguna del Maule volcanic field of the Andean southern volcanic zone (Chile) 2007–2012. *Geophysical Journal International*, *196*(2), 885–901. https://doi.org/10.1093/gji/ggt438

Grove, T. L., Till, C. B., & Krawczynski, M. J. (2012). The role of H_2O in subduction zone magmatism. *Annual Review of Earth and Planetary Sciences*, *40*(1), 413–439. https://doi.org/10.1146/annurev-earth-042711-105310

Hacker, B. R. (2008). H_2O subduction beyond arcs. *Geochemistry, Geophysics, Geosystems*, *9*, Q03001. https://doi.org/10.1029/2007GC001707

Hacker, B. R., Peacock, S. M., Abers, G. A., & Holloway, S. D. (2003). Subduction factory 2. Are intermediate-depth earthquakes in subducting slabs linked to metamorphic dehydration reactions? *Journal of Geophysical Research*, 2030. https://doi.org/10.1029/2001JB001129

Hata, M., Oshiman, N., Yoshimura, R., Tanaka, Y., & Uyeshima, M. (2015). Three-dimensional electromagnetic imaging of upwelling fluids in the Kyushu subduction zone Japan. *Journal of Geophysical Research: Solid Earth*, *120*, 1–17. https://doi.org/10.1002/2014JB011336

Hayes, G. P., Wald, D. J., & Johnson, R. L. (2012). Slab1.0: A three-dimensional model of global subduction zone geometries. *Journal of Geophysical Research*, *117*, B01302. https://doi.org/10.1029/2011JB008524

Heise, W., Grant Caldwell, T., Bannister, S., Bertrand, E. A., Ogawa, Y., Bennie, S. L., & Ichihara, H. (2017). Mapping subduction interface coupling using magnetotellurics: Hikurangi margin, New Zealand. *Geophysical Research Letters*, *44*, 9261–9266. https://doi.org/10.1002/2017GL074641

Heise, W., & Pous, J. (2003). Anomalous phases exceeding 90 degrees in magnetotellurics: Anisotropic model studies and a field example. *Geophysical Journal International*, *155*(1), 308–318. https://doi.org/10.1046/j.1365-246X.2003.02050.x

Hensen, C., Wallmann, K., Schmidt, M., Ranero, C. R., & Suess, E. (2004). Fluid expulsion related to mud extrusion off Costa Rica—A window to the subducting slab. *Geology*, *32*(3), 201–204. https://doi.org/10.1130/G20119.1

Hervé, F., Calderón, M., Fanning, C. M., Pankhurst, R. J., & Godoy, E. (2013). Provenance variations in the Late Paleozoic accretionary complex of central Chile as indicated by detrital zircons. *Gondwana Research*, *23*(3), 1122–1135. https://doi.org/10.1016/j.gr.2012.06.016

Hicks, S. P., Rietbrock, A., Haberland, C. A., Ryder, I. M. A., Simons, M., & Tassara, A. (2012). The 2010 Mw 8.8 Maule, Chile earthquake: Nucleation and rupture propagation controlled by a subducted topographic high. *Geophysical Research Letters*, *39*, L08310. https://doi.org/10.1029/2012GL053184

Hicks, S. P., Rietbrock, A., Ryder, I. M. A., Lee, C., & Miller, M. (2014). Anatomy of a megathrust: The 2010 M8.8 Maule, Chile earthquake rupture zone imaged using seismic tomography. *Earth and Planetary Science Letters*, *405*, 142–155. https://doi.org/10.1016/j.epsl.2014.08.028

Hickson, C. J., Ferraris, F., Rodriquez, C., Sielfeld, G., Henriquez, R., Gislason, T., et al. (2011). The Mariposa Geothermal System Chile. *Geothermal Resources Council Transactions*, *35*, 817–826.

Hildreth, W., & Moorbath, S. (1988). Crustal contributions to arc magmatism in the Andes of central Chile. *Contributions to Mineralogy and Petrology*, *98*(4), 455–489. https://doi.org/10.1007/BF00372365

Hyndman, R. D., & Peacock, S. M. (2003). Serpentinization of the forearc mantle. *Earth and Planetary Science Letters*, *212*(3-4), 417–432. https://doi.org/10.1016/S0012-821X(03)00263-2

Hyndman, R. D., Yamano, Y., & Oleskevich, D. A. (1997). The seismogenic zone of subduction thrust faults. *Island Arc*, *6*(3), 244–260. https://doi.org/10.1111/j.1440-1738.1997.tb00175.x

IRIS Data Services (2018). IRIS interactive earthquake browser: Web interface. Retrieved from: https://www.iris.edu/hq/, (Accessed 5 March, 2018).

Jödicke, H., Jording, A., Ferrari, L., Arzate, J., Mezger, K., & Rüpke, L. (2006). Fluid release from the subducted Cocos plate and partial melting of the crust deduced from magnetotelluric studies in southern Mexico: Implications for the generation of volcanism and subduction dynamics. *Journal of Geophysical Research*, *111*, B08102. https://doi.org/10.1029/2005JB003739

van Keken, P. E., Hacker, B. R., Syracuse, E. M., & Abers, G. A. (2011). Subduction factory: 4. Depth-dependent flux of H_2O from subducting slabs worldwide. *Journal of Geophysical Research*, *116*, B01401. https://doi.org/10.1029/2010JB007922

Kerrick, D. M. Y., & Connolly, J. A. D. (2001). Metamorphic devolatilization of subducted oceanic metabasalts: Implications for seismicity, arc magmatism and volatile recycling. *Earth and Planetary Science Letters*, *189*(1-2), 19–29. https://doi.org/10.1016/S0012-821X(01)00347-8

Larsen, J. C., Mackie, R. L., Manzella, A., Fiordelisi, A., & Rieven, S. (1996). Robust smooth magnetotelluric transfer functions. *Geophysical Journal International*, *124*(3), 801–819. https://doi.org/10.1111/j.1365-246X.1996.tb05639.x

Laske, G., Masters, G., Ma, Z., & Pasyanos, M. E. (2013). Update on CRUST1.0: A 1-degree global model of Earth's crust, in: EGU2013-2658. In *Geophysical research abstracts* (Vol. 15, p. 2658). Vienna, Austria: EGU General Assembly.

Lay, T., Kanamori, H., Ammon, C. J., Koper, K. D., Hutko, A. R., Ye, L., et al. (2012). Depth-varying rupture properties of subduction zone megathrust faults. *Journal of Geophysical Research*, *117*, B04311. https://doi.org/10.1029/2011JB009133

Le Mével, H., Feigl, K. L., Cõrdova, L., DeMets, C., & Lundgren, P. (2015). Evolution of unrest at Laguna del Maule volcanic field (Chile) from InSAR and GPS measurements, 2003 to 2014. *Geophysical Research Letters*, *42*, 6590–6598. https://doi.org/10.1002/2015GL064665

Lin, Y. N., Sladen, A., Ortega-culaciati, F., Simons, M., Avouac, J., Fielding, E. J., et al. (2013). Coseismic and postseismic slip associated with the 2010 Maule earthquake, Chile: Characterizing the Arauco Peninsula barrier effect. *Journal of Geophysical Research: Solid Earth*, *118*, 3142–3159. https://doi.org/10.1002/jgrb.50207

Mackie, R., & Madden, T. (1993). Three-dimensional magnetotelluric inversion using conjugate gradients. *Geophysical Journal International*, *115*(1), 215–229. https://doi.org/10.1111/j.1365-246X.1993.tb05600.x

Maksymowicz, A., Tréhu, A. M., Contreras-reyes, E., & Ruiz, S. (2015). Density-depth model of the continental wedge at the maximum slip segment of the Maule Mw 8.8 megathrust earthquake. *Earth and Planetary Science Letters*, *409*, 265–277. https://doi.org/10.1016/j.epsl.2014.11.005

Mardia, K. (1972). *Statistics of directional data, probability and mathematical statistics: A series of monographs and textbooks*. Academic Press. https://doi.org/10.1016/B978-0-12-471150-1.50008-X

McGary, R., Evans, R., & Wannamaker, P. (2014). Pathway from subducting slab to surface for melt and fluids beneath Mount Rainier. *Nature*, *511*(7509), 338–340. https://doi.org/10.1038/nature13493

McNeice, G., & Jones, A. (2001). Multisite, multifrequency tensor decomposition of magnetotelluric data. *Geophysics*, *66*(1), 158–173. https://doi.org/10.1190/1.1444891

Moreno, M., Haberland, C., Oncken, O., Rietbrock, A., Angiboust, S., & Heidbach, O. (2014). Locking of the Chile subduction zone controlled by fluid pressure before the 2010 earthquake. *Nature Geoscience*, *7*(4), 292–296. https://doi.org/10.1038/NGEO2102

Moreno, M., Li, S., Melnick, D., Bedford, J., Baez, J., Motagh, M., et al. (2018). Chilean megathrust earthquake recurrence linked to frictional contrast at depth. *Nature Geoscience*, *11*(4), 285–290. https://doi.org/10.1038/s41561-018-0089-5

Moreno, M., Melnick, D., Rosenau, M., Baez, J., Klotz, J., Oncken, O., et al. (2012). Toward understanding tectonic control on the Mw 8.8 2010 Maule Chile earthquake. *Earth and Planetary Science Letters*, *321-322*, 152–165. https://doi.org/10.1016/j.epsl.2012.01.006

Moscoso, E., Grevemeyer, I., Contreras-reyes, E., Flueh, E. R., Dzierma, Y., Rabbel, W., & Thorwart, M. (2011). Revealing the deep structure and rupture plane of the 2010 Maule, Chile earthquake (Mw = 8.8) using wide angle seismic data. *Earth and Planetary Science Letters*, *307*(1-2), 147–155. https://doi.org/10.1016/j.epsl.2011.04.025

Peacock, S. M. (1990). Fluid processes in subduction zones. *Science*, *248*(4953), 329–337. https://doi.org/10.1126/science.248.4953.329

Pesicek, J. D., Engdahl, E. R., Thurber, C. H., DeShon, H. R., & Lange, D. (2012). Mantle subducting slab structure in the region of the 2010 M8.8 Maule earthquake (30–40°S), Chile. *Geophysical Journal International*, *191*(1), 317–324. https://doi.org/10.1111/j.1365-246X.2012.05624.x

Petrelli, M., El Omari, K., Spina, L., Le Guer, Y., La Spina, G., & Perugini, D. (2018). Timescales of water accumulation in magmas and implications for short warning times of explosive eruptions. *Nature Communications*, *9*(1), 770. https://doi.org/10.1038/s41467-018-02987-6

Poli, S., & Schmidt, M. W. (1995). H_2O transport and release in subduction zones: Experimental constraints on basaltic and andesitic systems. *Journal of Geophysical Research*, *100*, 299–314.

Pommier, A., & Evans, R. L. (2017). Constraints on fluids in subduction zones from electromagnetic data. *Geosphere*, *13*, 1–16. https://doi.org/10.1130/GES01473.1

Pritchard, M. E., Jay, J. A., Aron, F., Henderson, S. T., & Lara, L. E. (2013). Subsidence at southern Andes volcanoes induced by the 2010 Maule, Chile earthquake. *Nature Geoscience*, *6*(8), 632–636. https://doi.org/10.1038/ngeo1855

Ramos, V. A., & Folguera, A. (2011). Payenia volcanic province in the southern Andes: An appraisal of an exceptional Quaternary tectonic setting. *Journal of Volcanology and Geothermal Research*, *201*(1-4), 53–64. https://doi.org/10.1016/j.jvolgeores.2010.09.008

Ramos, V. A., Litvak, V. D., Folguera, A., & Spagnuolo, M. (2014). An Andean tectonic cycle: From crustal thickening to extension in a thin crust (34°–37° SL). *Geoscience Frontiers*, *5*(3), 351–367. https://doi.org/10.1016/j.gsf.2013.12.009

Reyes-Wagner, V., Díaz, D., Cordell, D., & Unsworth, M. (2017). Regional electrical structure of the Andean subduction zone in central Chile (35°–36°S) using magnetotellurics. *Earth, Planets and Space*, *69*(1), –9. https://doi.org/10.1186/s40623-017-0726-z

Rietbrock, A., Ryder, I., Hayes, G., Haberland, C., Comte, D., Roecker, S., & Lyon-Caen, H. (2012). Aftershock seismicity of the 2010 Maule Mw = 8.8, Chile, earthquake: Correlation between co-seismic slip models and aftershock distribution? *Geophysical Research Letters*, *39*, L08310. https://doi.org/10.1029/2012GL051308

Rodi, W., & Mackie, R. L. (2001). Nonlinear conjugate gradients algorithm for 2-D magnetotelluric inversion. *Geophysics*, *66*(1), 174–187. https://doi.org/10.1190/1.1444893

Ruiz, S., & Madariaga, R. (2018). Historical and recent large megathrust earthquakes in Chile. *Tectonophysics*, *733*, 37–56. https://doi.org/10.1016/j.tecto.2018.01.015

Saffer, D. M. (2017). Mapping fluids to subduction megathrust locking and slip behavior. *Geophysical Research Letters*, *44*, 9337–9340. https://doi.org/10.1002/2017GL075381

Schellart, W. P., & Rawlinson, N. (2013). Global correlations between maximum magnitudes of subduction zone interface thrust earthquakes and physical parameters of subduction zones. *Physics of the Earth and Planetary Interiors*, *225*, 41–67. https://doi.org/10.1016/j.pepi.2013.10.001

Schmidt, M. W., & Poli, S. (1998). Experimentally based water budgets for dehydrating slabs and consequences for arc magma generation. *Earth and Planetary Science Letters*, *163*(1-4), 361–379. https://doi.org/10.1016/S0012-821X(98)00142-3

Selway, K., Thiel, S., & Key, K. (2012). A simple 2-D explanation for negative phases in TE magnetotelluric data. *Geophysical Journal International*, *188*(3), 945–958. https://doi.org/10.1111/j.1365-246X.2011.05312.x

Singer, B. S., Thompson, R. A., Dungan, M. A., Feeley, T. C., Nelson, S. T., Pickens, J., et al. (1997). Volcanism and erosion during the past 930 ky at the Tatara–San Pedro complex, Chilean Andes. *GSA Bulletin*, *109*(2), 127–142. https://doi.org/10.1130/0016-7606(1997)109<0127:VAEDTP>2.3.CO;2

Sodoudi, F., Yuan, X., Asch, G., & Kind, R. (2011). High-resolution image of the geometry and thickness of the subducting Nazca lithosphere beneath northern Chile. *Journal of Geophysical Research*, *116*, B04302. https://doi.org/10.1029/2010JB007829

Soyer, W., & Unsworth, M. (2006). Deep electrical structure of the northern Cascadia (British Columbia, Canada) subduction zone: Implications for the distribution of fluids. *Geology*, *34*(1), 53–56. https://doi.org/10.1130/G21951.1

Stern, R. J. (2002). Subduction zones. *Reviews of Geophysics*, *40*(4), 1012. https://doi.org/10.1029/2001RG000108

Unsworth, M.J., Chira, J., Yupa, R., Antayhua-Vera, Y., Calla-Pilco, D., Baca, B. G., et al. (2018). Magnetotelluric studies of the Andean subduction zone in southern Peru, in: American Geophysical Union 2018 Fall Meeting.

Vargas, J. A., Meqbel, N. M., Ritter, O., Brasse, H., Weckmann, U., & Godoy, B. (2019). Fluid distribution in the central Andes subduction zone imaged with magnetotellurics. *Journal of Geophysical Research: Solid Earth*. https://doi.org/10.1029/2018JB016933

Völker, D., Kutterolf, S., & Wehrmann, H. (2011). Comparative mass balance of volcanic edifices at the southern volcanic zone of the Andes between 33°S and 46°S. *Journal of Volcanology and Geothermal Research*, *205*(3-4), 114–129. https://doi.org/10.1016/j.jvolgeores.2011.03.011

Völker, D., & Stipp, M. (2015). Water input and water release from the subducting Nazca Plate along southern central Chile (33°S–46°S). *Geochemistry, Geophysics, Geosystems*, *16*, 1825–1847. https://doi.org/10.1002/2015GC005766

Wada, I., & Behn, M. D. (2015). Focusing of upward fluid migration beneath volcanic arcs: Effect of mineral grain size variation in the mantle wedge. *Geochemistry, Geophysics, Geosystems*, *16*, 3905–3923. https://doi.org/10.1002/2015GC005950

Wannamaker, P. E., Caldwell, T. G., Jiracek, G. R., Maris, V., Hill, G. J., Ogawa, Y., et al. (2009). Fluid and deformation regime of an advancing subduction system at Marlborough, New Zealand. *Nature*, *460*(7256), 733–736. https://doi.org/10.1038/nature08204

Wannamaker, P. E., Evans, R. L., Bedrosian, P. A., Unsworth, M. J., Maris, V., & McGary, R. S. (2014). Segmentation of plate coupling, fate of subduction fluids, and modes of arc magmatism in Cascadia, inferred from magnetotelluric resistivity. *Geochemistry, Geophysics, Geosystems*, *15*, 4230–4253. https://doi.org/10.1002/2014GC005509

Wespestad, C. E., Thurber, C. H., Andersen, N. L., Singer, B. S., Cardona, C., Zeng, X., et al. (2019). Magma reservoir below Laguna del Maule Volcanic Field, Chile imaged with surface-wave tomography. *Journal of Geophysical Research: Solid Earth*. https://doi.org/10.1029/2018JB016485

Wiese, H. (1962). Geomagnetische tiefensondierung. Teil II: Die Streichrichtung der Untergrundstrukturen des elektrischen Widerstandes, erschlossen aus geomagnetischen variationen. *Geofisica Pura e Applicata*, *52*(1), 83–103. https://doi.org/10.1007/BF01996002

Wilson, C. R., Spiegelman, M., van Keken, P. E., & Hacker, B. R. (2014). Fluid flow in subduction zones: The role of solid rheology and compaction pressure. *Earth and Planetary Science Letters*, *401*, 261–274. https://doi.org/10.1016/j.epsl.2014.05.052

Worzewski, T., Jegen, M., Kopp, H., Brasse, H., & Taylor Castillo, W. (2011). Magnetotelluric image of the fluid cycle in the Costa Rican subduction zone. *Nature Geoscience*, *4*(2), 108–111. https://doi.org/10.1038/ngeo1041